Supplemental Material to:

Discontinuous transtensional rupture during the Mw 7.2, 1995 Gulf of Aqaba earthquake

H. Vasyura-Bathke[1,2,3], A. Steinberg[4], F. Krüger[2], G. Feng[5], P.M. Mai[1], S. Jónsson[1]

January 29, 2024

[1] King Abdullah University of Science and Technology, Thuwal 23955-6900, Saudi Arabia

[2] University of Potsdam, D-14476 Potsdam, Germany

[3] Now at: Helmholtz Centre Potsdam, German Research Centre for Geosciences GFZ

[4] BGR, Federal Institute for Geosciences and Natural Resources,
D-30655 Hannover, Germany

[5] Central South University, Changsha, China

1 Tables

Satellite	Direction	Primary	Secondary	Perp. Baseline	Track
ERS1	ascending	03/05/1995	23/05/1996	-90 m	T343
ERS1	ascending	16/08/1995	21/08/1997	-562 m	T114a
ERS1	ascending	20/11/1993	02/04/1996	-350 m	T114b
ERS1	descending	08/06/1995	23/05/1996	-50 m	T350
JERS	descending	03/11/1995	10/06/1996	2002 m	T254

Table S1: Interferometric pairs and SAR datasets used in the co-seismic rupture estimation. The data named 'T343off' shown in SAR data misfit figures (S5d, S12d, S16d, S21d) are amplitude offsets derived from the data of track T343.

Reference	Latitude [°]	Longitude [°]	Depth [km]	Strike [°]	Dip [°]	Rake [°]	Length [km]	Width [km]	Magnitude [Mw]
seismic									
[Pinar and Türkelli, 1997]	28.4	34.6	10	92	38	-58	-	-	6.55
	28.5	34.7	15	288	82	-164	-	-	6.99
								total:	7.04
Klinger et al. [1999]	28.829	34.825	18.8	191.6	58.6	-21.2	-	-	6.65
	29.042	34.777	18.65	199.3	74.3	-5	-	-	7.12
	29.277	34.786	5.15	24.7	67.2	-8.5	-	-	6.62
								total:	7.21
Hofstetter et al. [2003]	28.97	34.75	10	202	77	-15	50	30	7.2
geodetic									
Klinger et al. [2000]*	28.93	34.78	12	195.15	65.	-15.5	48	14	7.08
Baer et al. [2001]	28.96	34.73	15	197	80	-14	55	11	7.15
Shamir et al. [2003]*	28.975	34.77	13	200	80	-20	48	14	7.2
Baer et al. [2008]*	28.97	34.75	11.25	197.5	67	-4	58.5	30	7.18

Table S2: Previously estimated parameters of point and finite sources by using seismic or geodetic data. Note that some studies (marked with asterisk) used prior information as obtained by the other datasets to constrain their solution space.

2 Figures

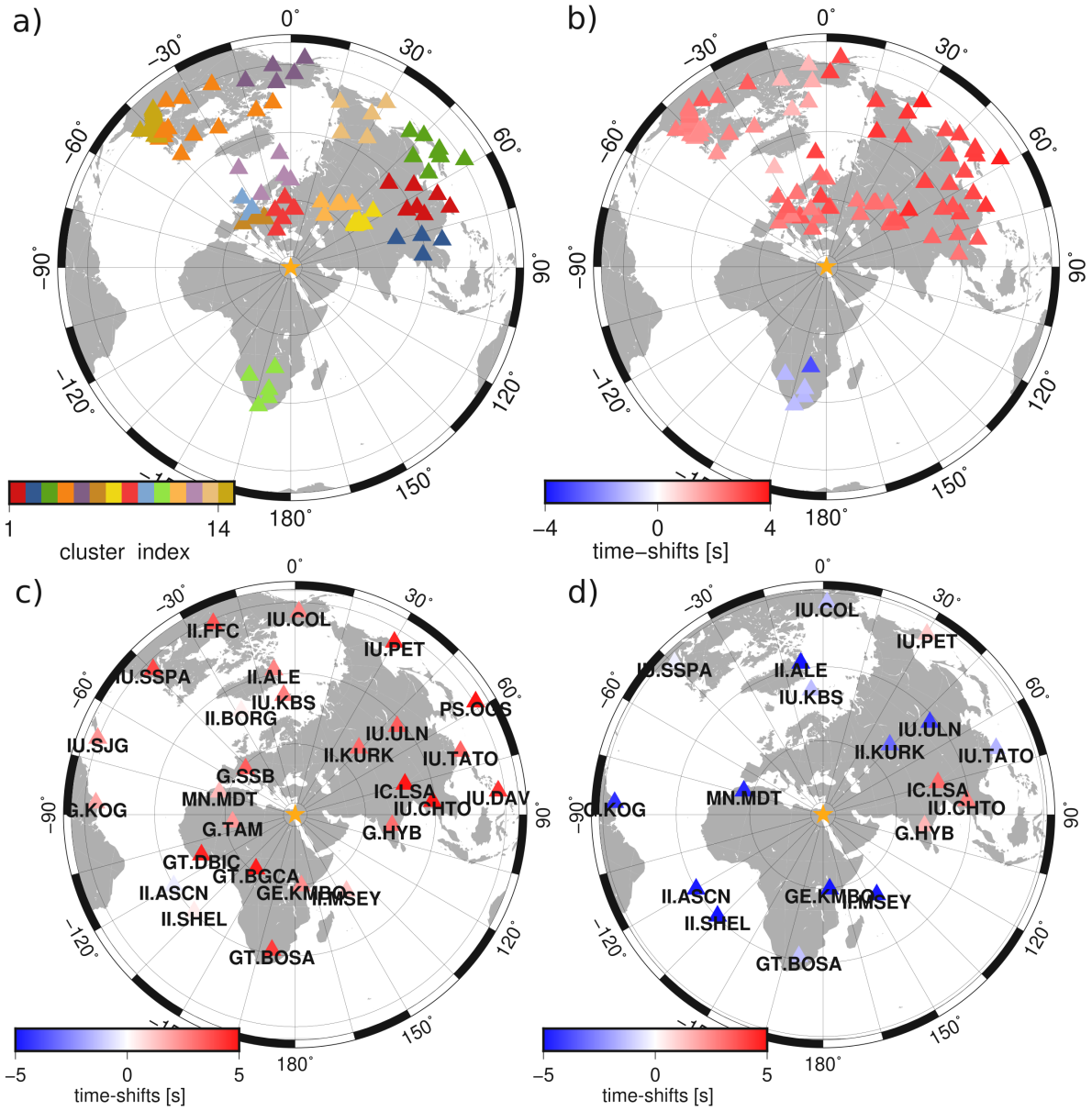

Figure S1: a) Teleseismic stations that are clustered to form virtual arrays for multi-array backprojection. b) Empirical traveltime correction calibrated with the location and source time from the Mw 5.7 aftershock from 23.11.1995 at 18:07:17. c) Teleseismic broadband stations used for the kinematic finite fault estimation for P-wave arrivals and d) for S-wave arrivals. Stations are colored with the station corrections hierarchically estimated in the Bayesian inference.

2.1 Geometry inference

2.2 Two sub-faults

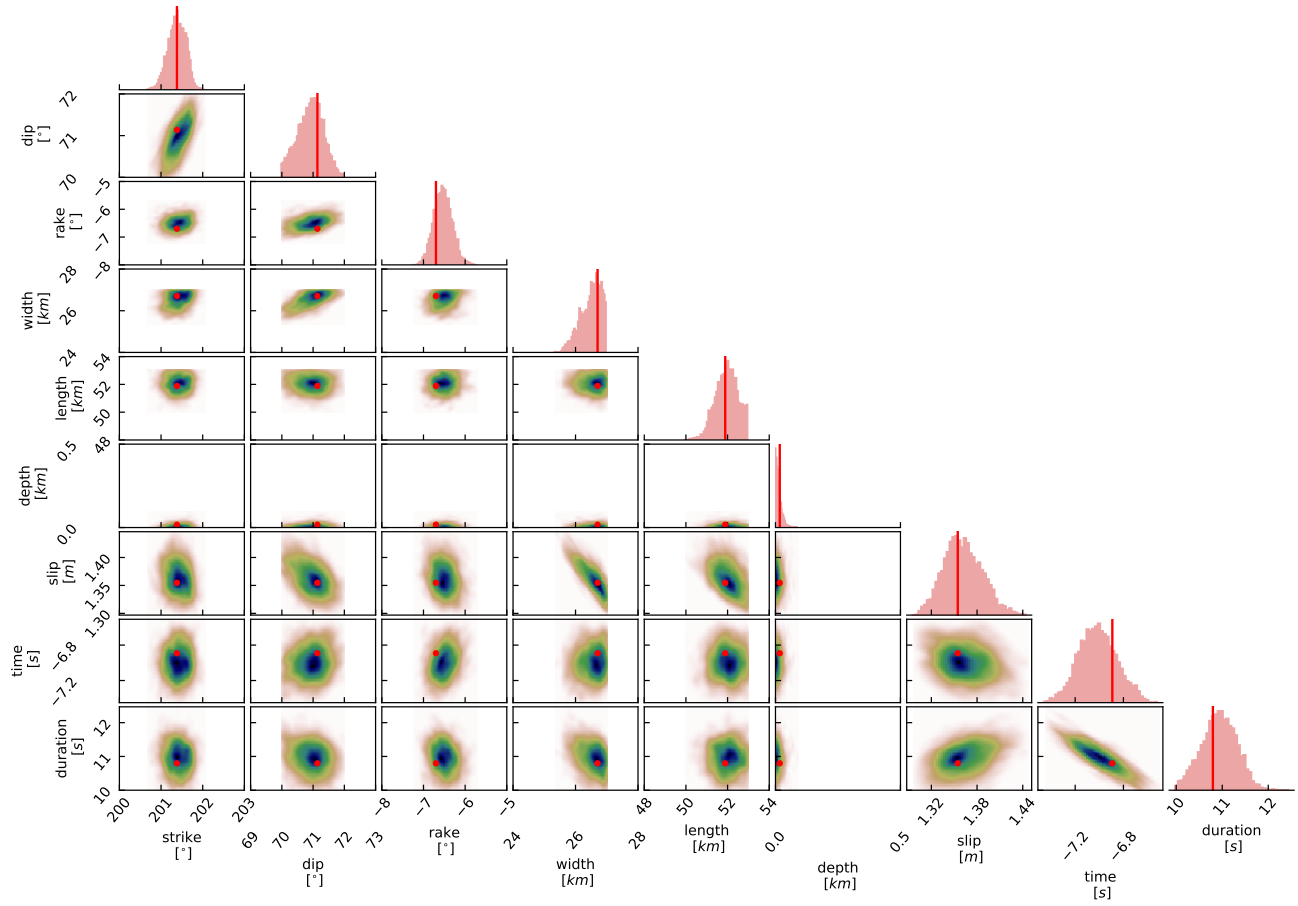

Figure S2: Two sub-faults: 1d and 2d marginal posteriors for the inferred geometry parameters of the first fault segment. Red vertical lines in the histograms and red dots in the correlation plots mark the maximum a-posteriori (MAP) solution. Blue colors in the correlation plots indicate parameters with high probability. The color of the histogram relates to the fault segment and coloring in Fig. 3.

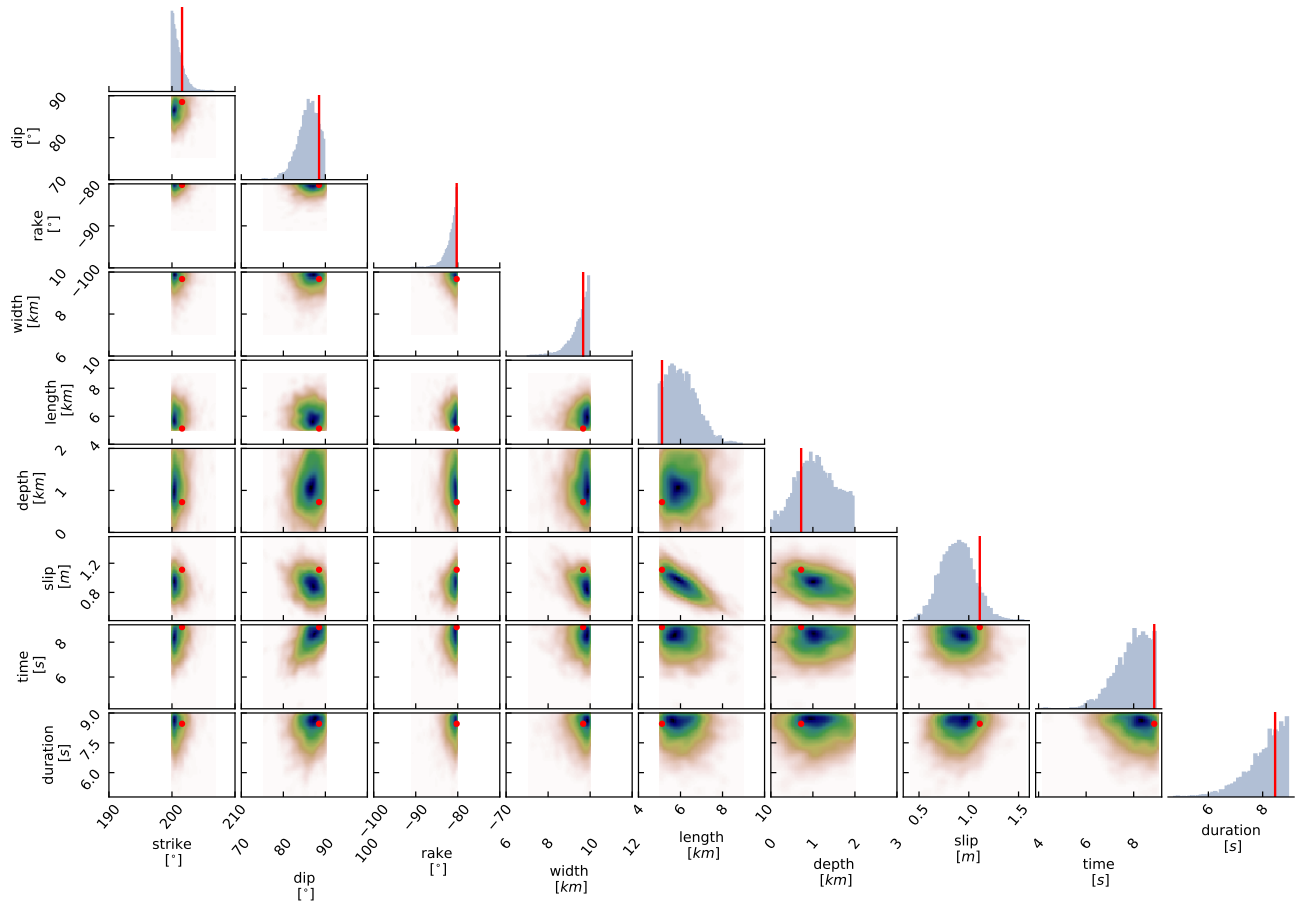

Figure S3: Two sub-faults: 1d and 2d marginals for the inferred fault geometry of the second fault segment. See caption of Fig. S2 for further details.

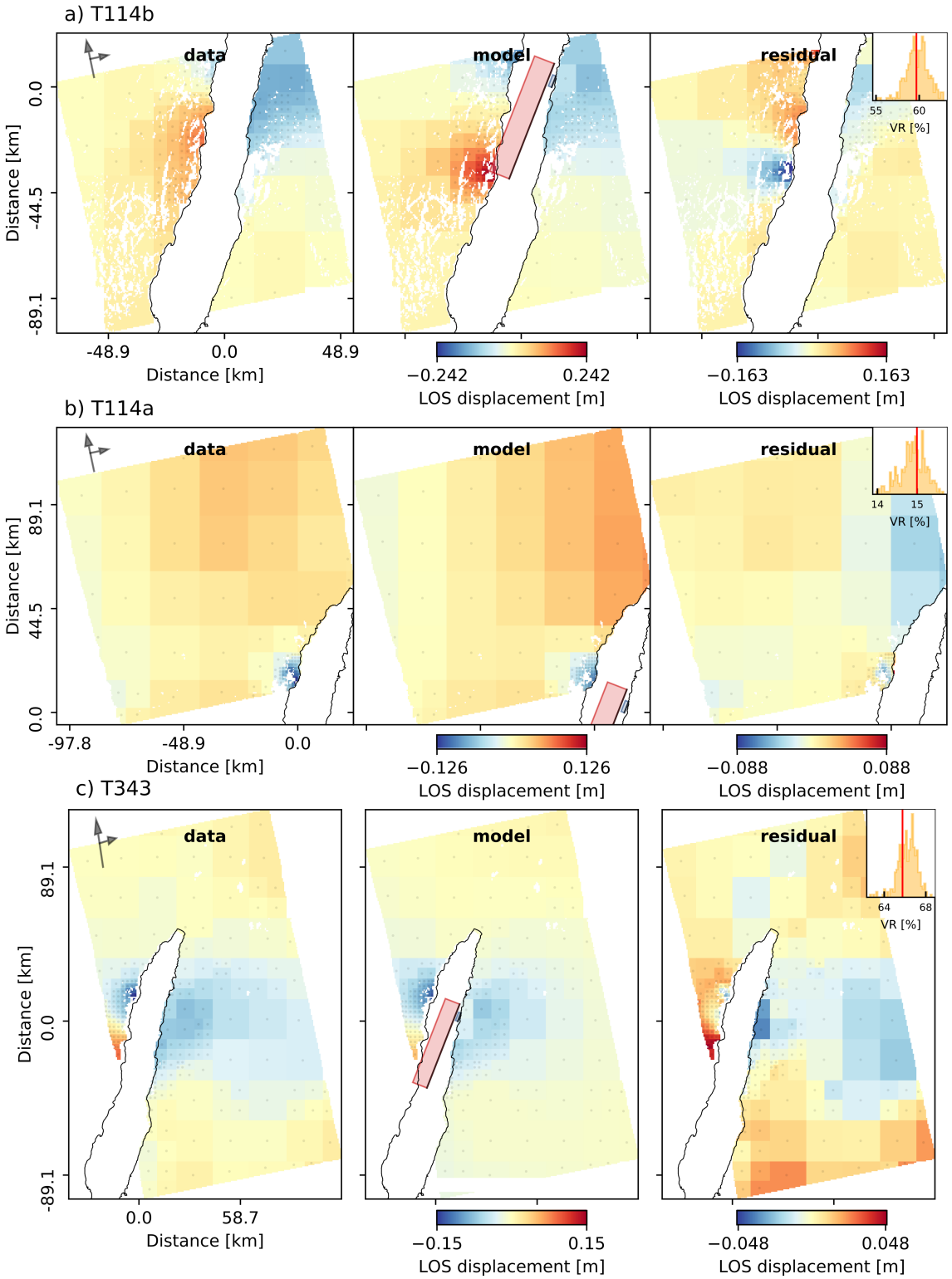

Figure S4: Two sub-faults: InSAR data fits for the geometry inference for the 1995 Gulf of Aqaba earthquake where a), b) and c) show the track numbers (see also Fig. 2, Tab.S1). (Data panels) Geocoded unwrapped interferograms in radar line-of-sight (LOS) where positive numbers indicate LOS distance decrease due to movement of the surface towards the satellite.

The displayed displacement values are the result of quadtree subsampling and they are extrapolated to pixels belonging to the same square. The long and short arrows show satellite flight direction and radar LOS direction, respectively. (Model panels) Synthetic LOS surface displacements derived from the MAP solution. The colored rectangles, red and blue show the locations and orientations of the western (first) and eastern (second) fault segments. (Residual panels) Difference between data and model panels, that is, the residual surface displacements; note the rescaled colormap. Top right shows a histogram of weighted variance reduction from the posterior ensemble of solutions, where the red vertical line marks the MAP solution.

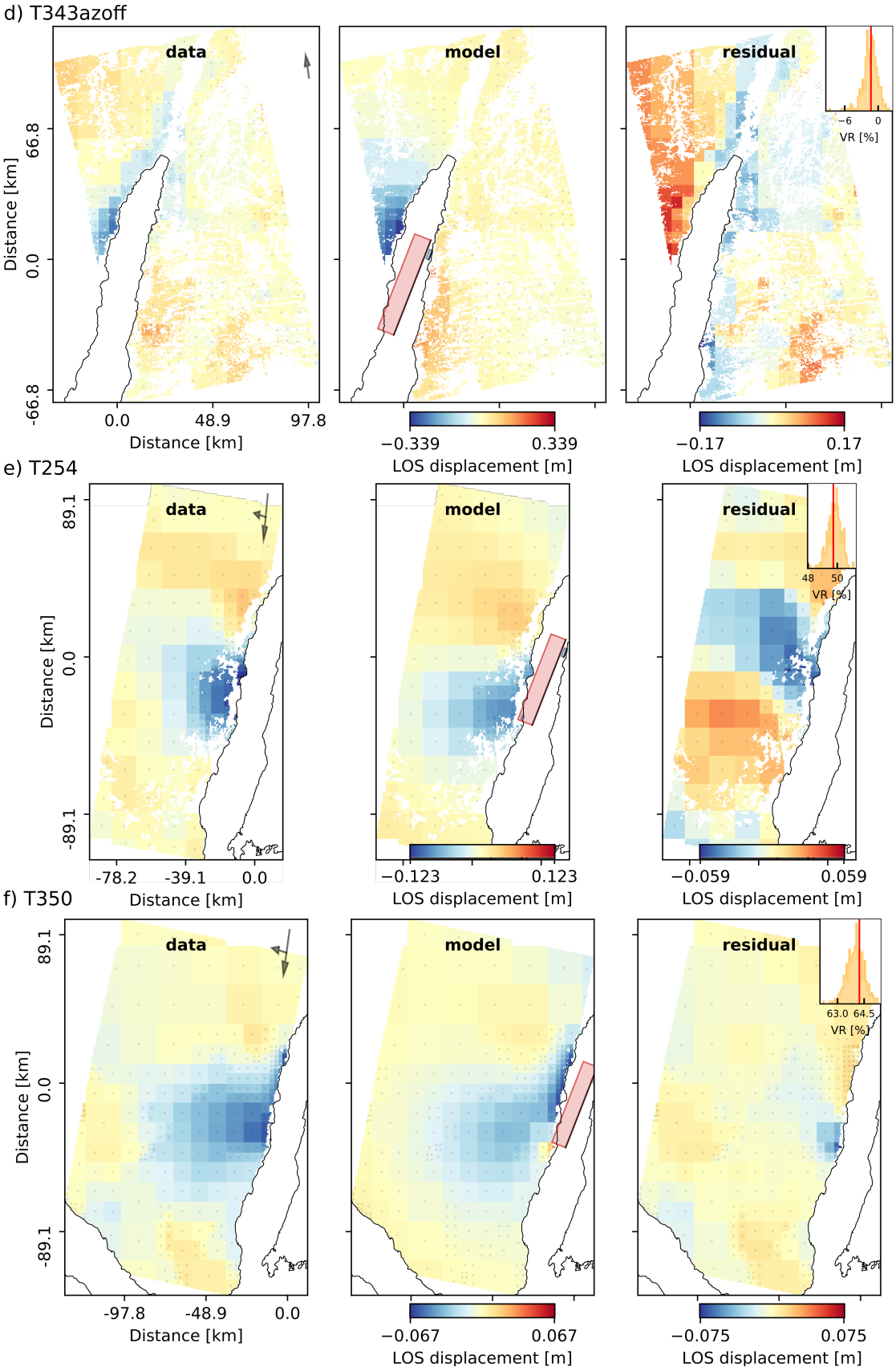

Figure S5: Two sub-faults: InSAR data fits for the geometry inference for the 1995 Gulf of Aqaba earthquake. Further details are given in the caption of Fig. S4

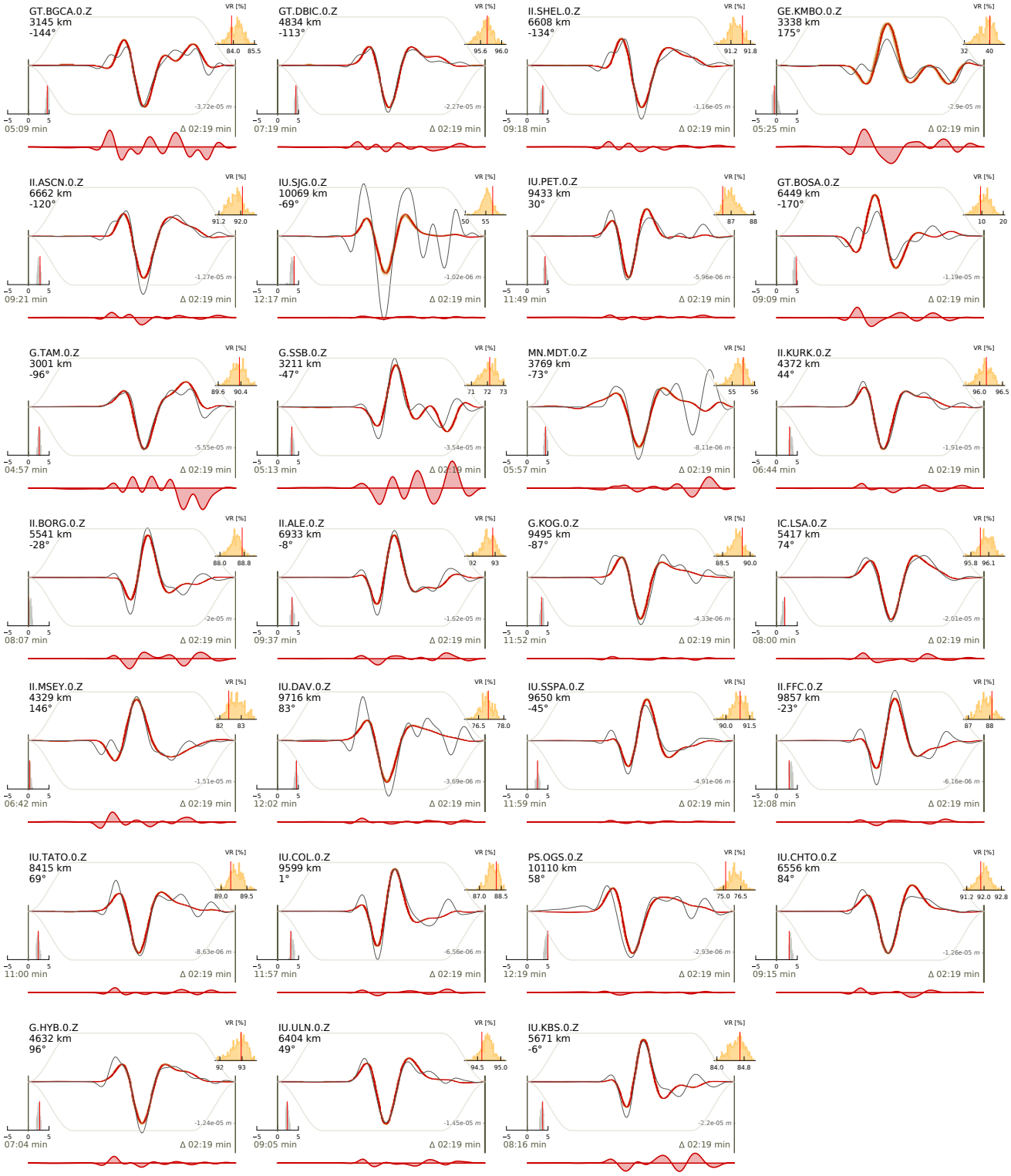

Figure S6: Two sub-faults: Waveform fits for the geometry inference of the 1995 Gulf of Aqaba earthquake. Solid gray lines show the filtered (0.01-0.05 Hz) data of the vertical component tapered around the P-wave arrival. The red continuous line shows the synthetic waveforms derived from the MAP solution, whereas, brownish shaded colors indicate synthetic waveforms derived from the full posterior ensemble of parameters. The residual waveforms between MAP and data are shown below as the filled red polygons.

Histograms in the top right and bottom left show weighted variance reduction and time-shifts in seconds, respectively. The vertical red lines mark the MAP solutions. Each trace-window is annotated by network name, station name, component, distance and azimuth. The wave arrival time and the duration of the windows are shown in the bottom left and right, respectively.

Figure S7: Two sub-faults: Waveform fits for the geometry inference of the 1995 Gulf of Aqaba earthquake. Solid gray lines show the filtered (0.01-0.05 Hz) data of the transverse component tapered around the S-wave arrival. Further details are given in the caption of Fig. S6.

2.3 Three sub-faults

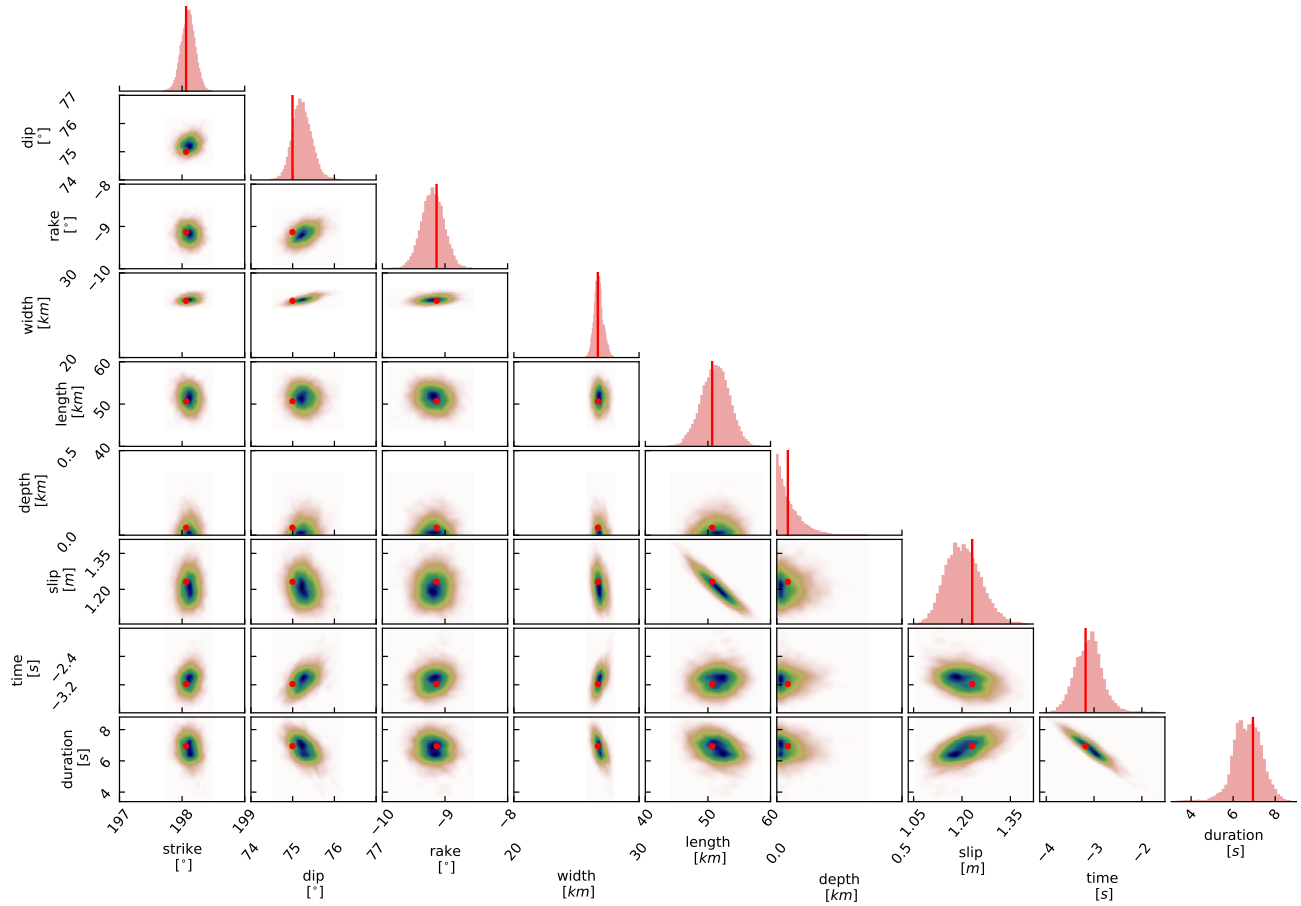

Figure S8: Three sub-faults: 1d and 2d marginal posteriors for the inferred geometry parameters of the first fault segment. Red vertical lines in the histograms and red dots in the correlation plots mark the maximum a-posteriori (MAP) solution. Blue colors in the correlation plots indicate parameters with high probability. The color of the histograms relate to the fault segment and coloring in Fig. 3, 4 (in the main text).

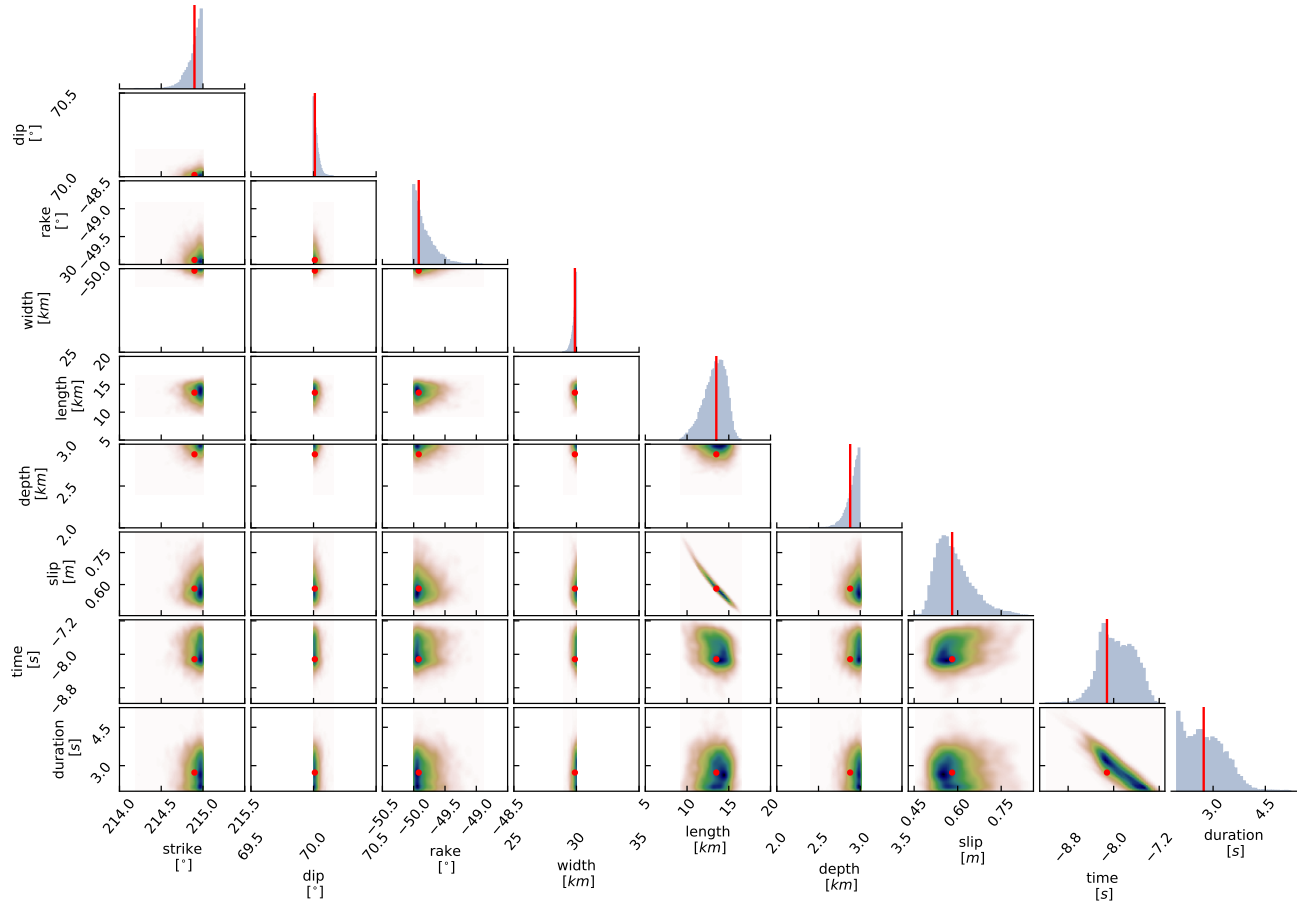

Figure S9: Three sub-faults: 1d and 2d marginals for the inferred fault geometry of the second fault segment. See caption of Fig. S8 for further details.

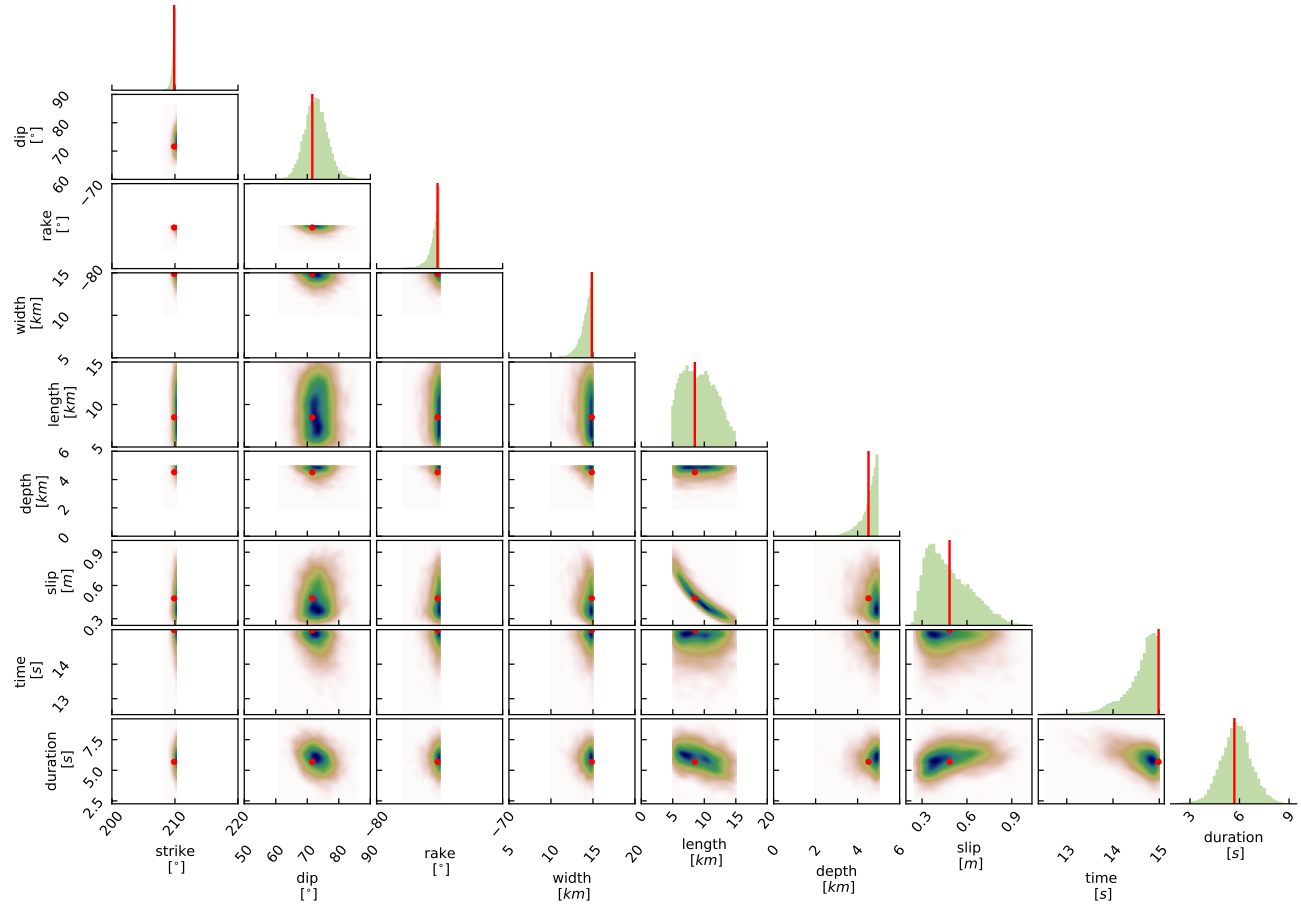

Figure S10: Three sub-faults: 1d and 2d marginals for the inferred fault geometry of the third fault segment. See caption of Fig. S8 for further details.

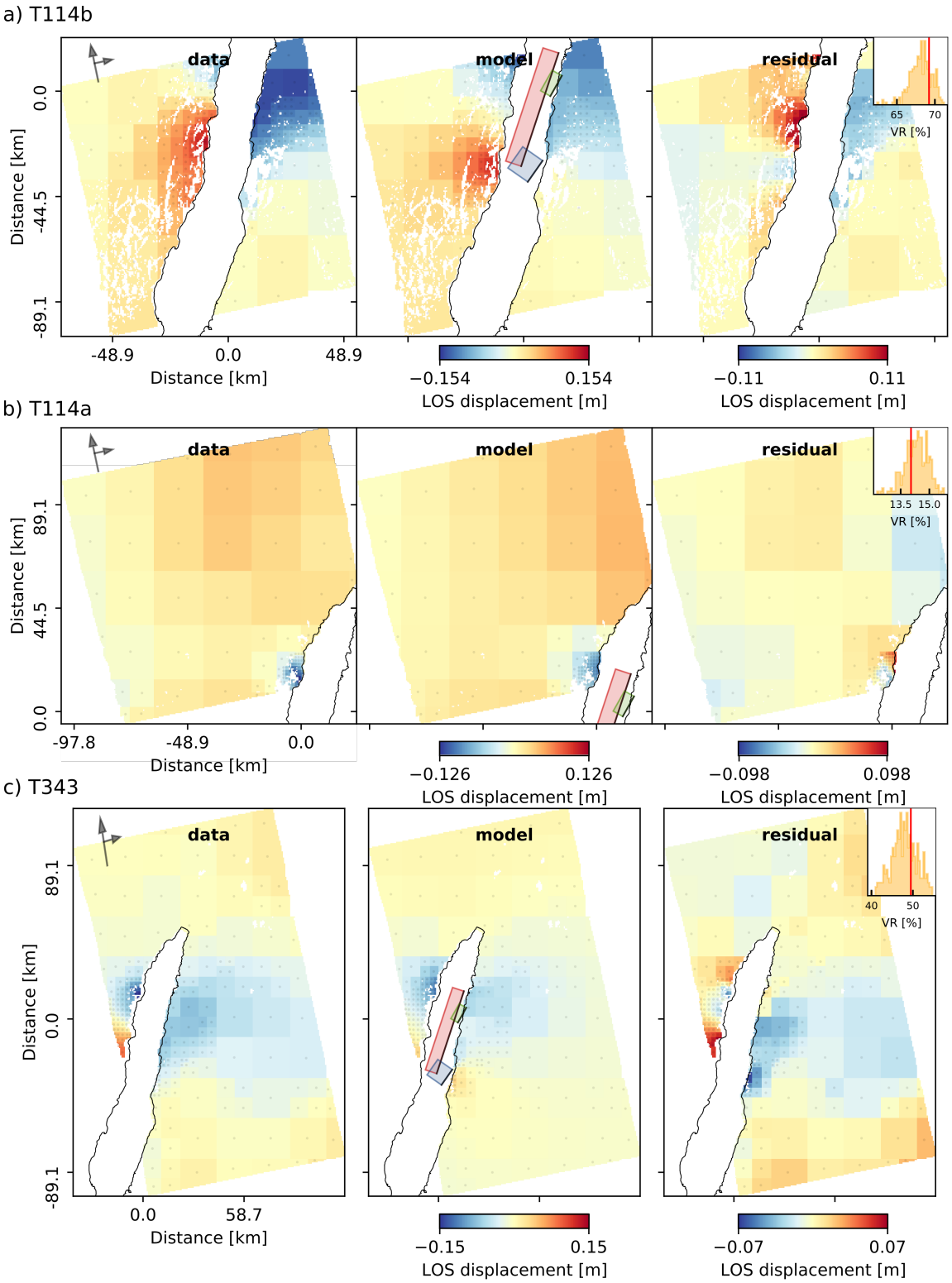

Figure S11: Three sub-faults: InSAR data fits for the geometry inference for the 1995 Gulf of Aqaba earthquake where a), b) and c) show the track numbers (see also Fig. 2, Tab.S1). (Data panels) Geocoded unwrapped interferograms in radar line-of-sight (LOS) where positive numbers indicate LOS distance decrease due to movement of the surface towards the satellite.

The displayed displacement values are the result of quadtree subsampling and they are extrapolated to pixels belonging to the same square. The long and short arrows show satellite flight direction and radar LOS direction, respectively. (Model panels) Synthetic LOS surface displacements derived from the MAP solution. The colored rectangles, blue, red and green show the locations and orientations of the southern (first), northern (second) and eastern (third) fault segments. (Residual panels) Difference between data and model panels, that is, the residual surface displacements; note the rescaled colormap. Top right shows a histogram of weighted variance reduction from the posterior ensemble of solutions, where the red vertical line marks the MAP solution.

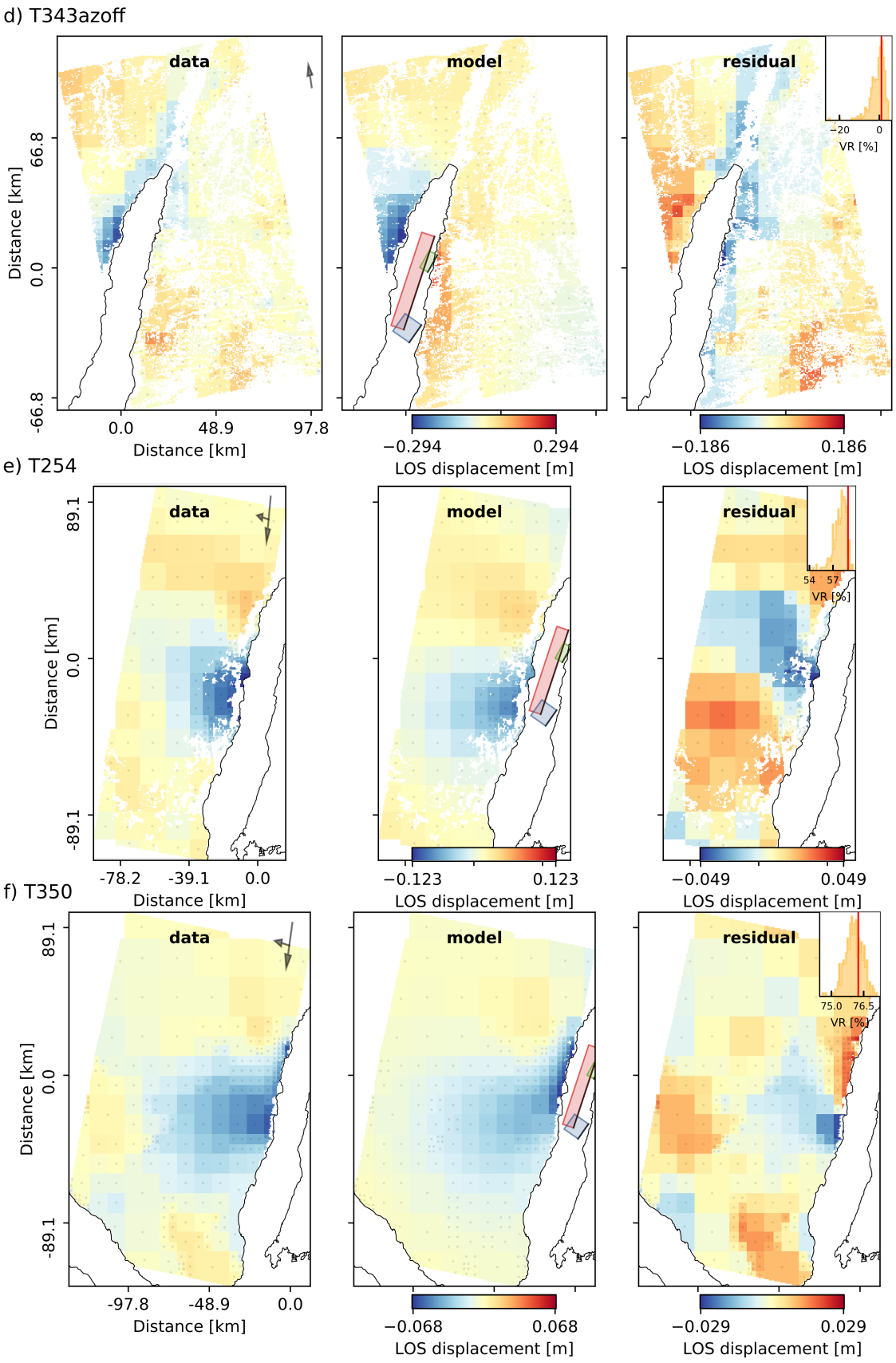

Figure S12: InSAR data fits for the geometry inference for the 1995 Gulf of Aqaba earthquake. Further details are given in the caption of Fig. S11.

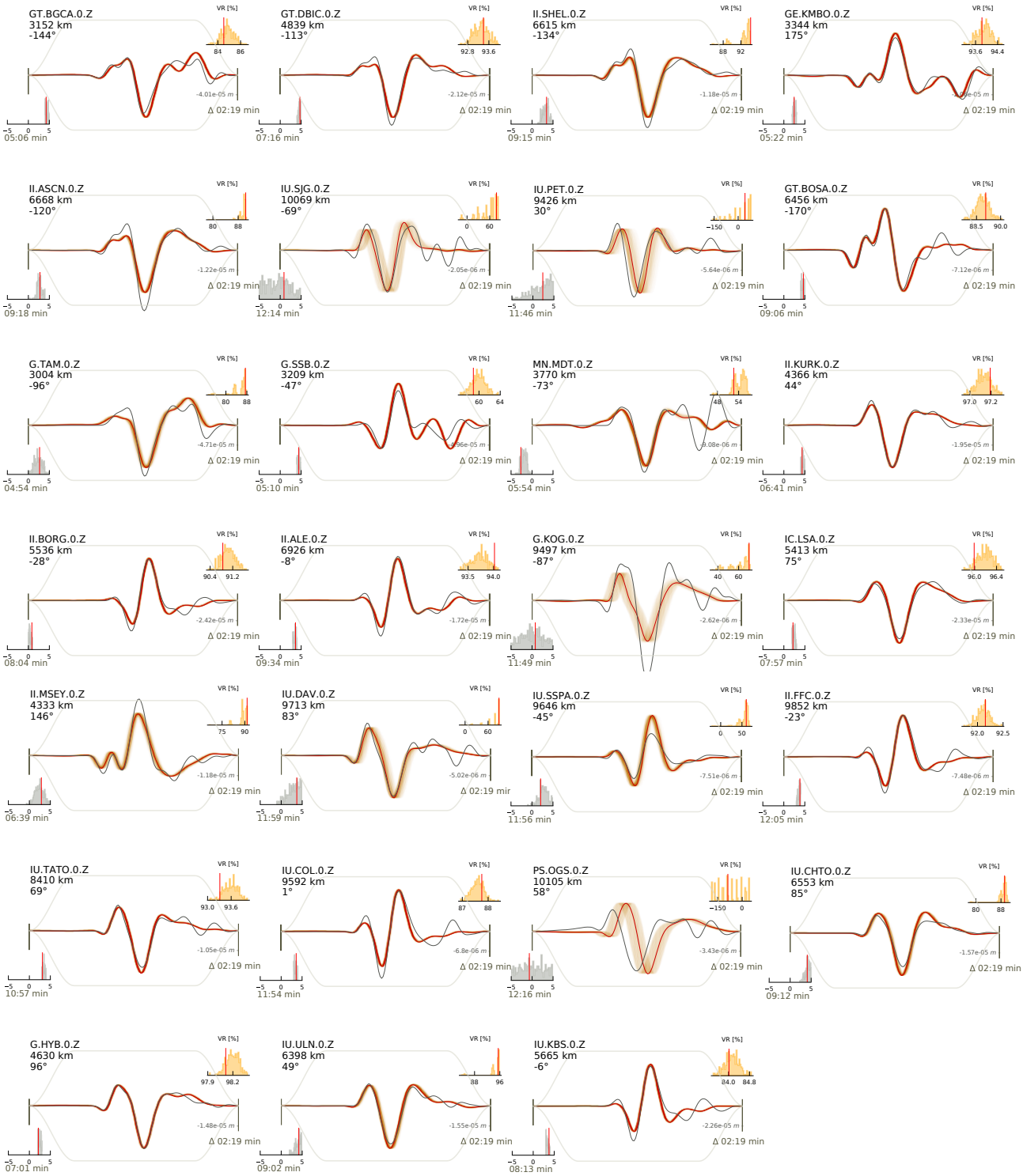

Figure S13: Three sub-faults: Waveform fits for the geometry inference of the 1995 Gulf of Aqaba earthquake. Further details are given in the caption of Fig. S6.

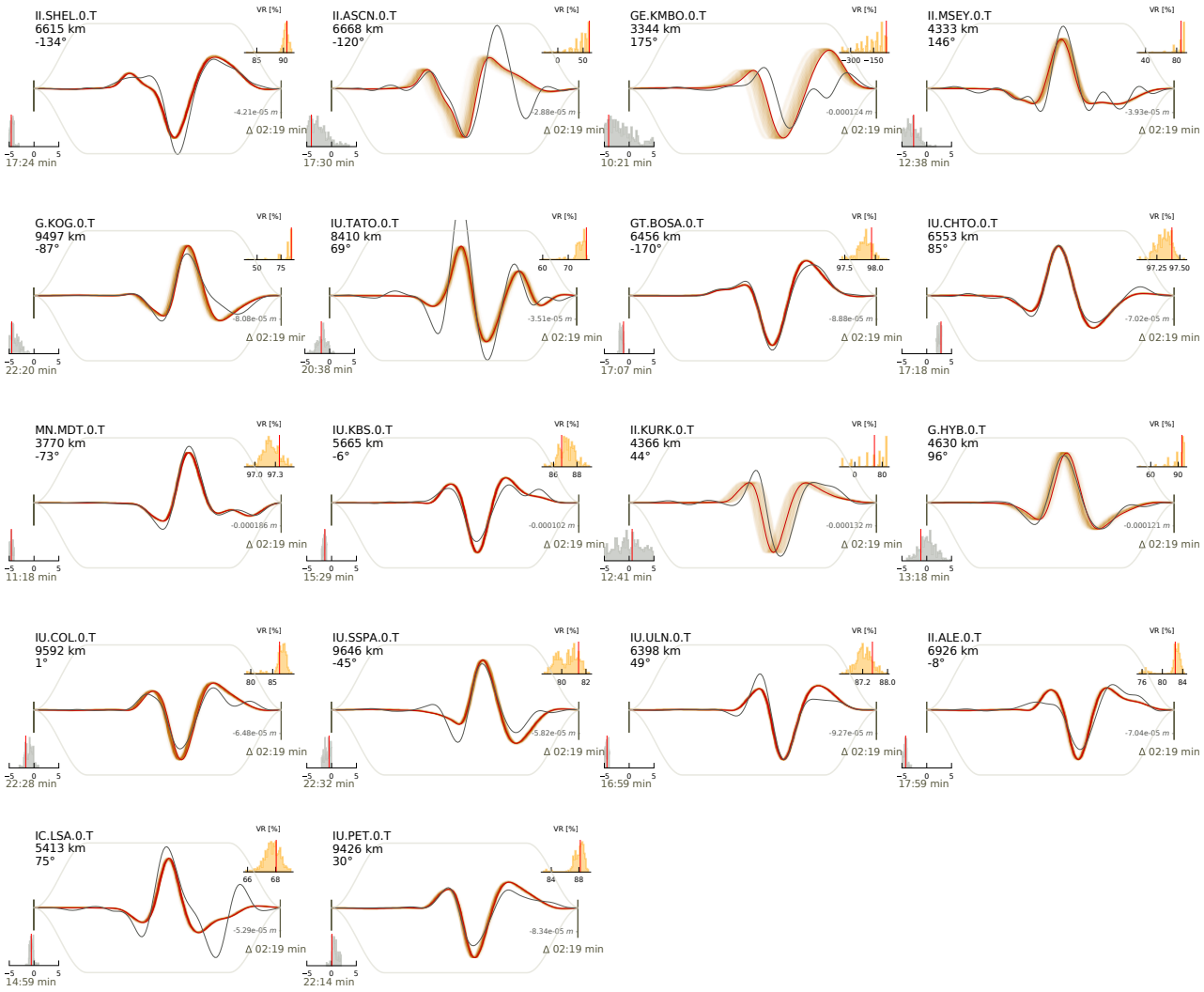

Figure S14: Three sub-faults: Waveform fits for the geometry inference of the 1995 Gulf of Aqaba earthquake. Solid gray lines show the filtered (0.01-0.05 Hz) data of the transverse component tapered around the S-wave arrival. Further details are given in the caption of Fig. S6.

17 **2.4 Finite fault inference**

18 **2.5 Two sub-faults**

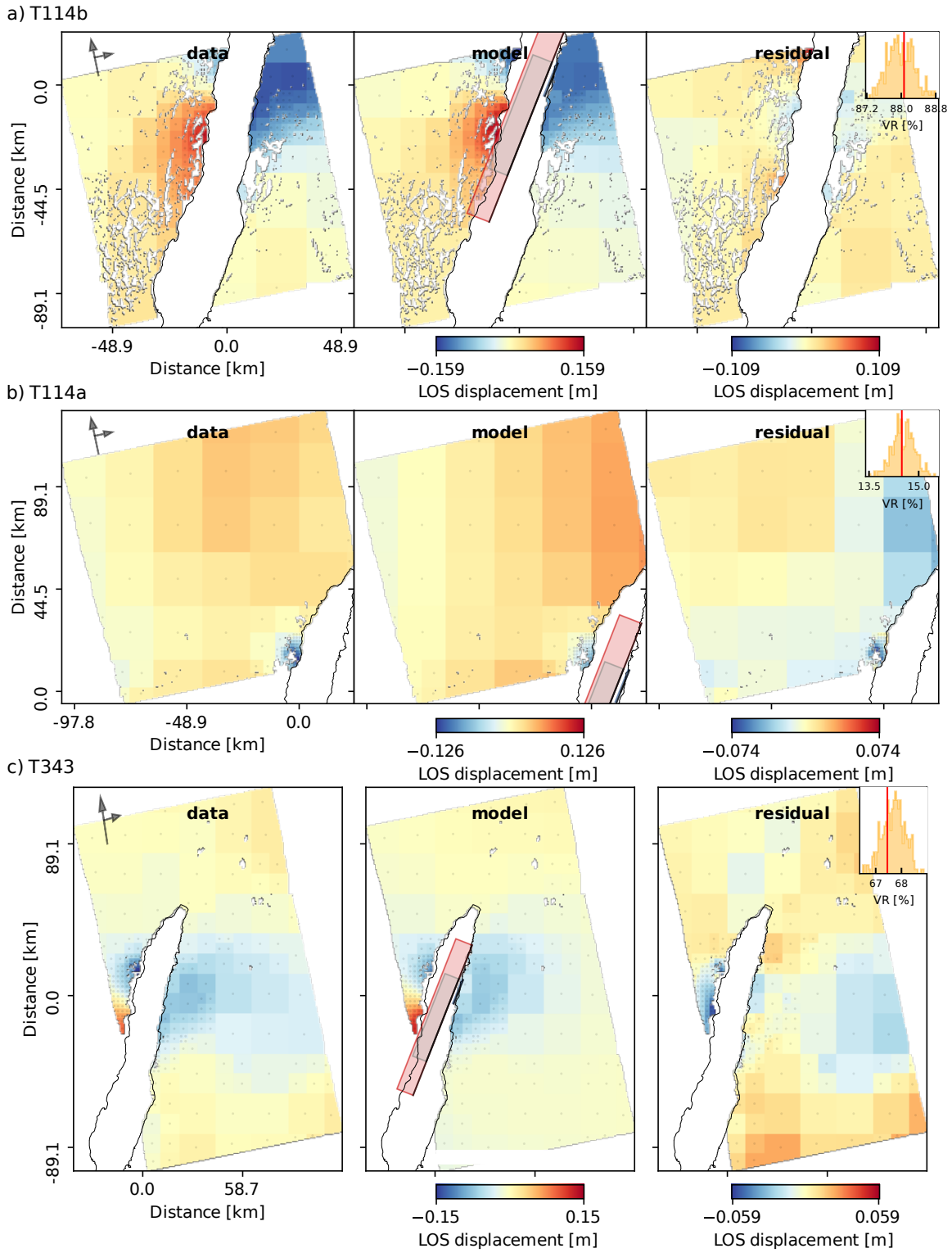

Figure S15: Two sub-faults: InSAR data fits for the finite-fault inference for the 1995 Gulf of Aqaba earthquake. Further details are given in the caption of Fig. S11. Note that the colored rectangles show the location and orientation of the reference faults that were extended from the previously determined MAP solution of the geometry inference (Fig. S4).

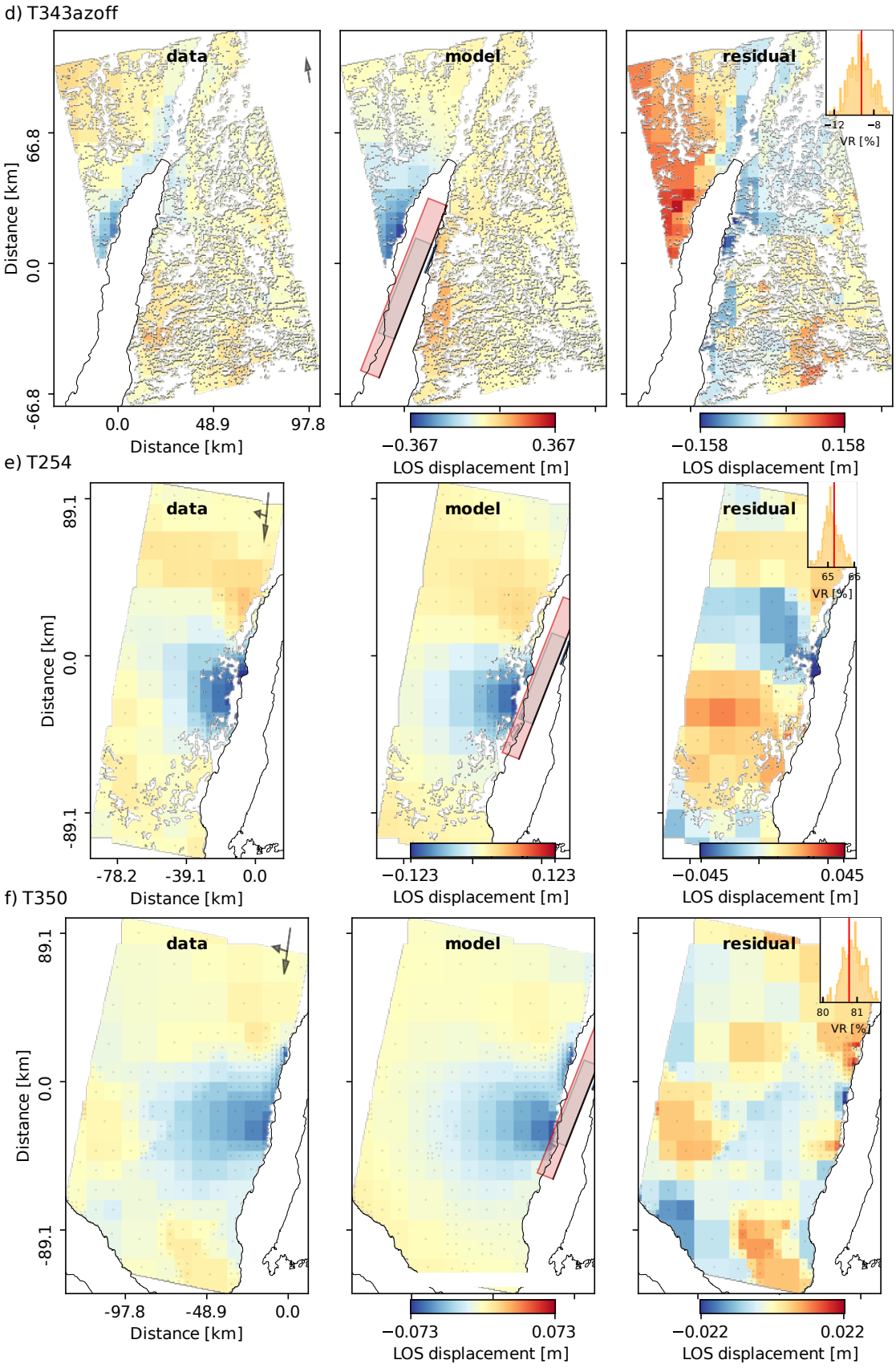

Figure S16: Two sub-faults: InSAR data fits for the finite-fault inference for the 1995 Gulf of Aqaba earthquake. Further details are given in the caption of Fig. S11.

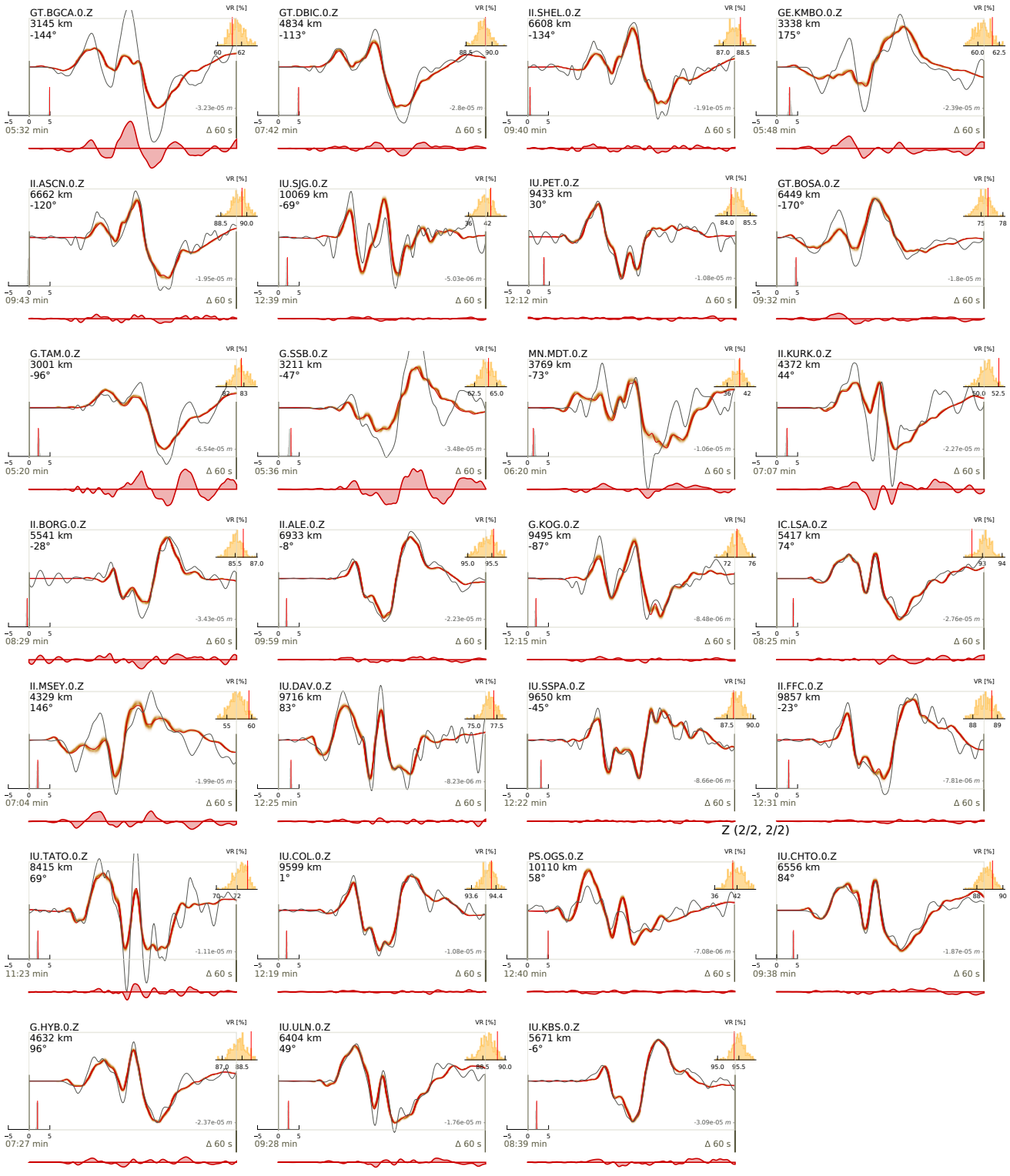

Figure S17: Two sub-faults: Waveform fits for the finite-fault inference of the 1995 Gulf of Aqaba earthquake. Solid gray lines show the filtered (0.01-0.5 Hz) data of the vertical component tapered around the P-wave arrival. Further details are given in the caption of Fig. S6.

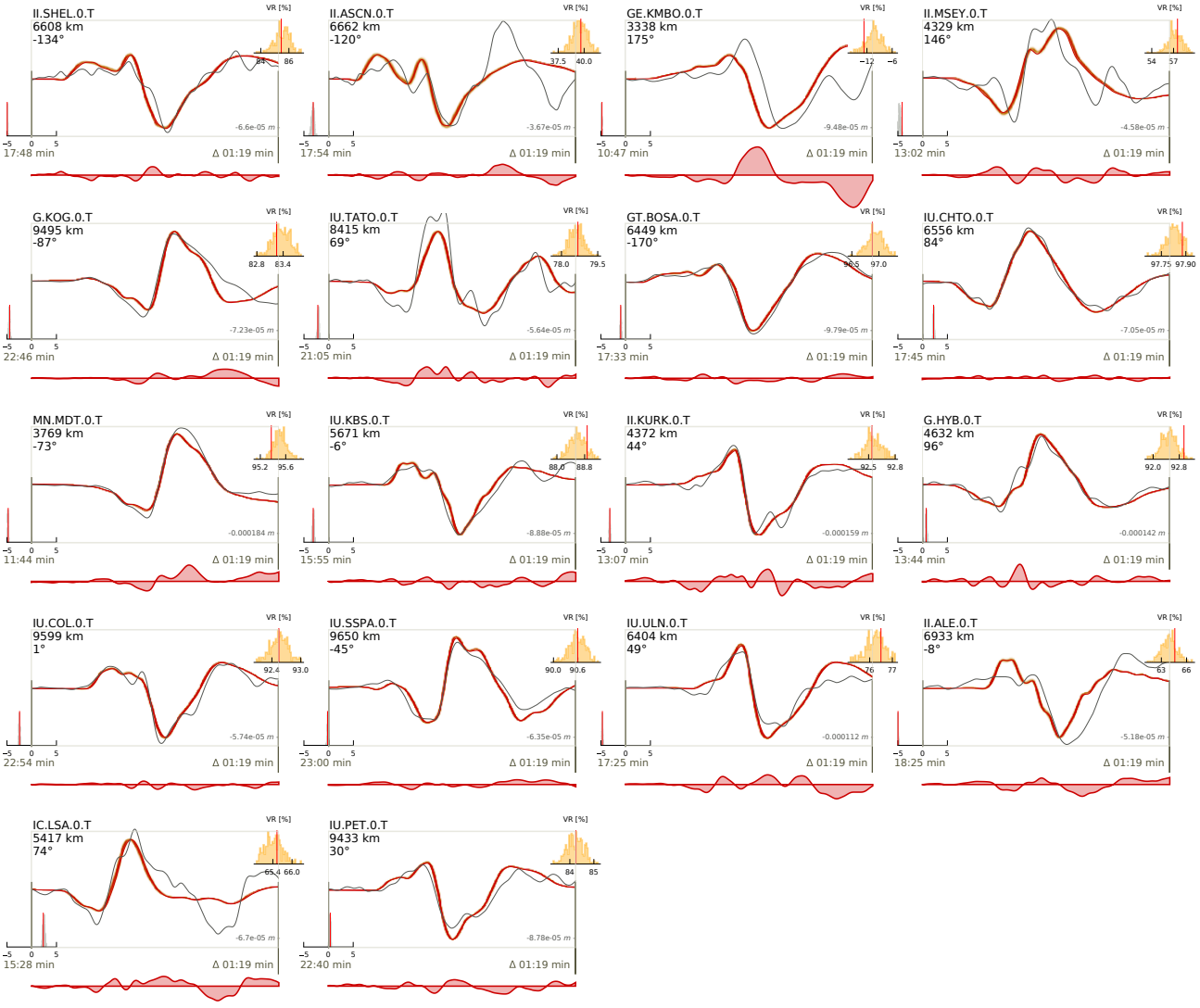

Figure S18: Two sub-faults: Waveform fits for the finite-fault inference of the 1995 Gulf of Aqaba earthquake. Solid gray lines show the filtered (0.01-0.5 Hz) data of the transverse component tapered around the S-wave arrival. Further details are given in the caption of Fig. S6.

2.6 Three sub-faults

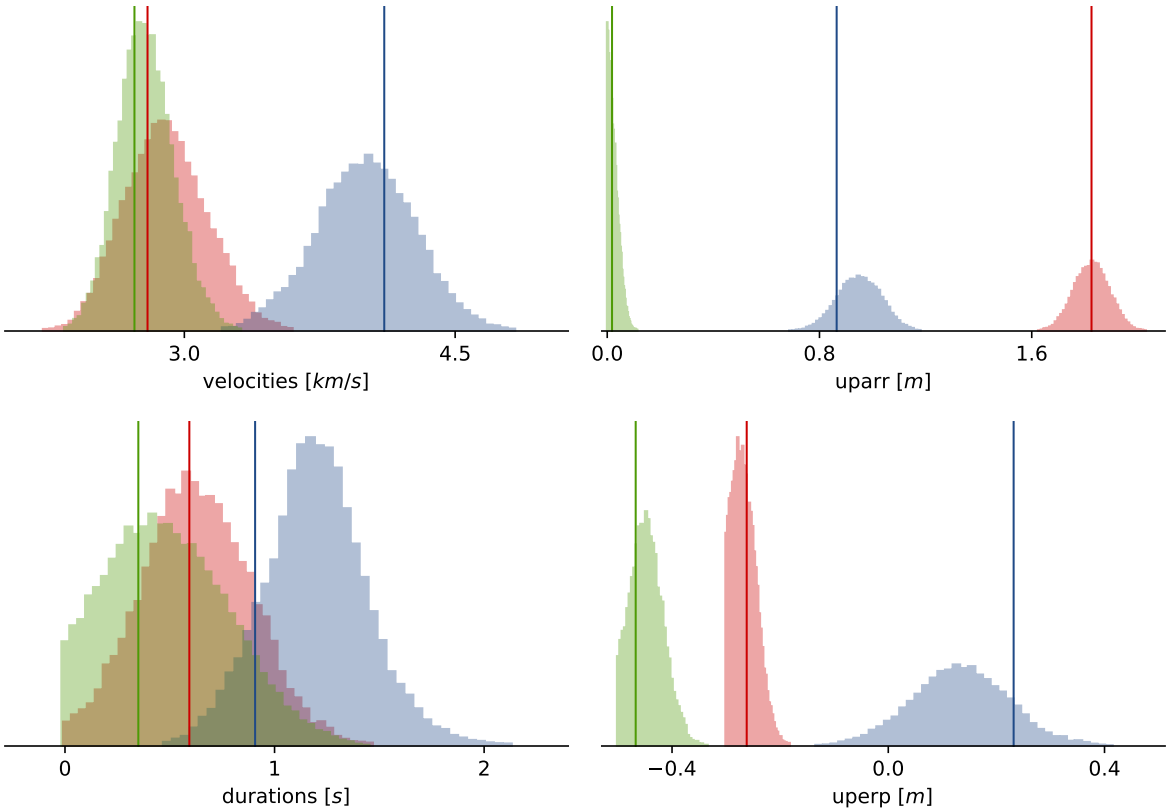

Figure S19: 1d marginals for selected patches (26-red, 124-blue, 145-green) of the distributed finite-fault inference. Vertical lines mark the MAP solutions. Note that the priors for the rupture velocity was limited to S-wave velocity, which is 4.7 km/s.

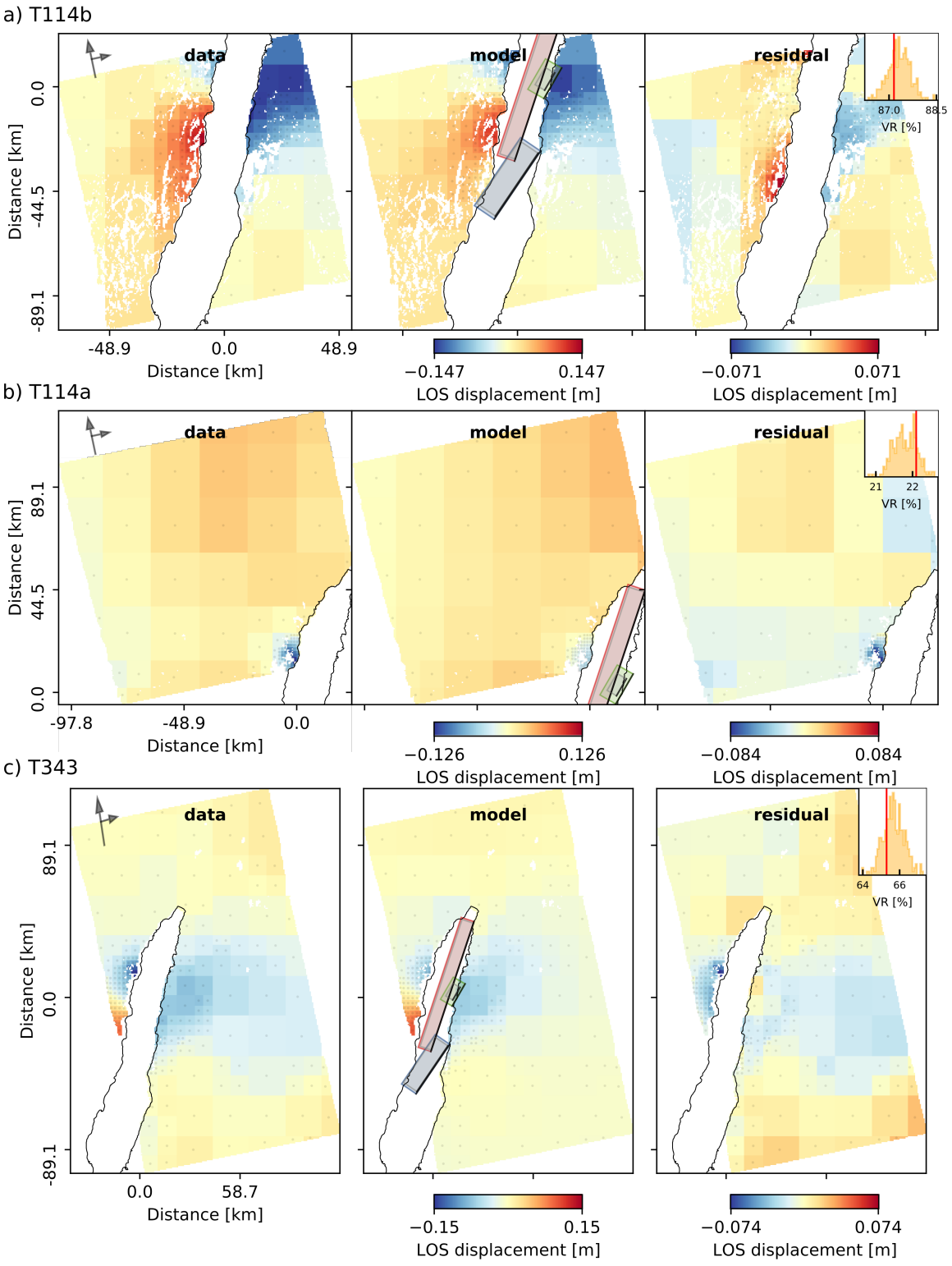

Figure S20: Three sub-faults: InSAR data fits for the finite-fault inference for the 1995 Gulf of Aqaba earthquake. Further details are given in the caption of Fig. S11. Note that the colored rectangles show the location and orientation of the reference faults that were extended from the previously determined MAP solution of the geometry inference (Fig. S11).

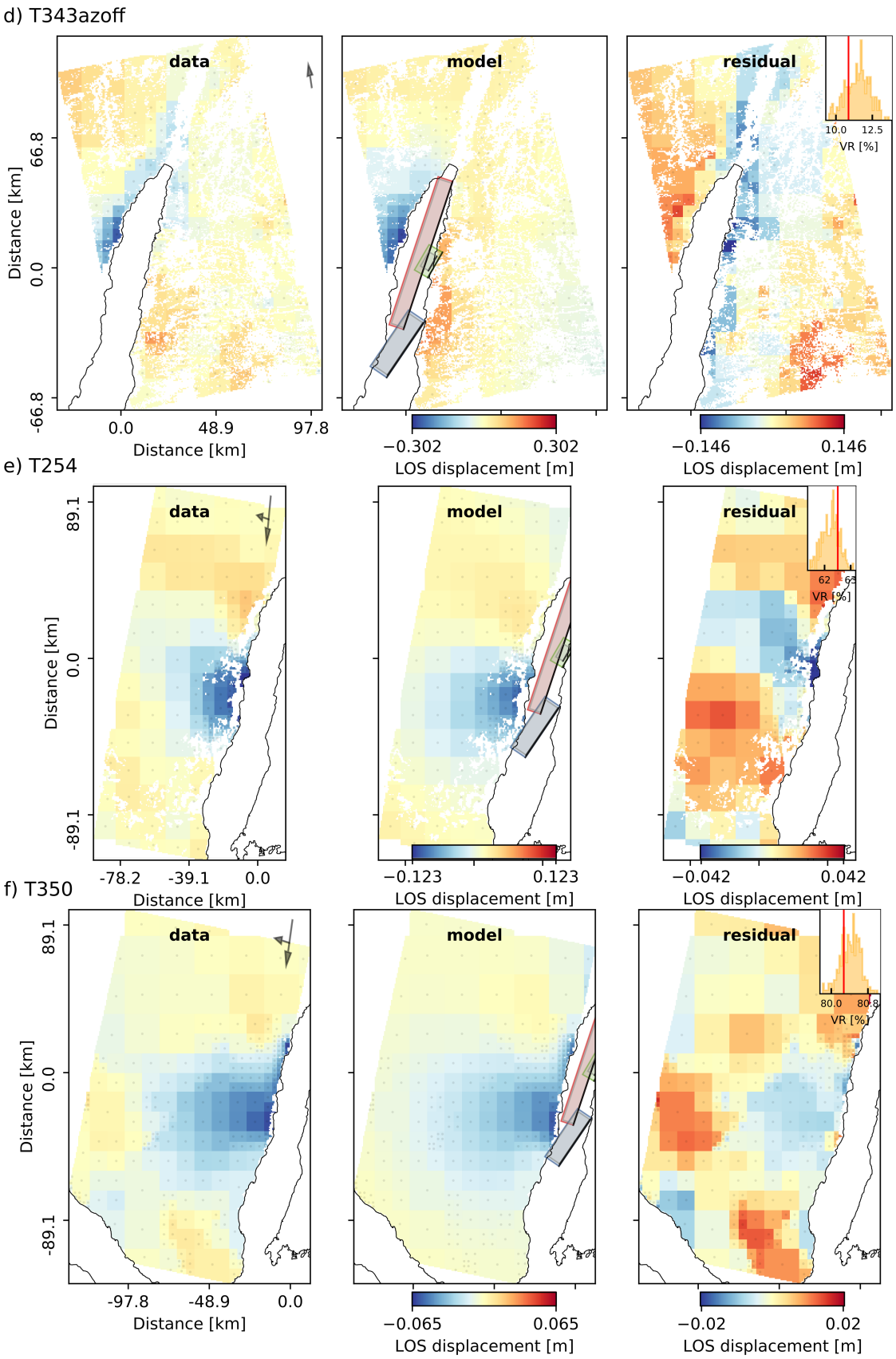

Figure S21: Three sub-faults: InSAR data fits for the finite-fault inference for the 1995 Gulf of Aqaba earthquake. Further details are given in the caption of Fig. S11.

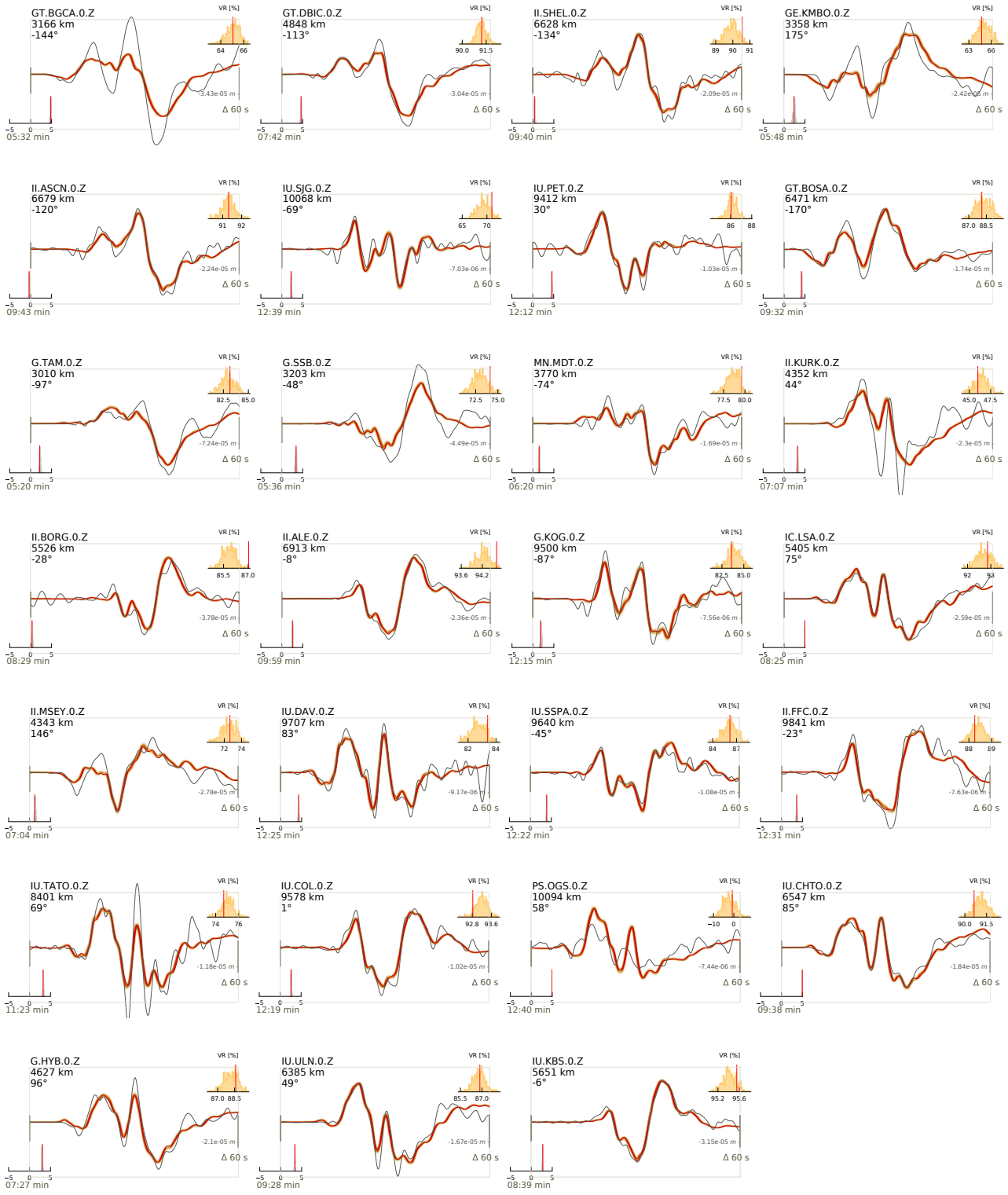

Figure S22: Three sub-faults: Waveform fits for the finite-fault inference of the 1995 Gulf of Aqaba earthquake. Solid gray lines show the filtered (0.01-0.5 Hz) data of the vertical component tapered around the P-wave arrival. Further details are given in the caption of Fig. S13.

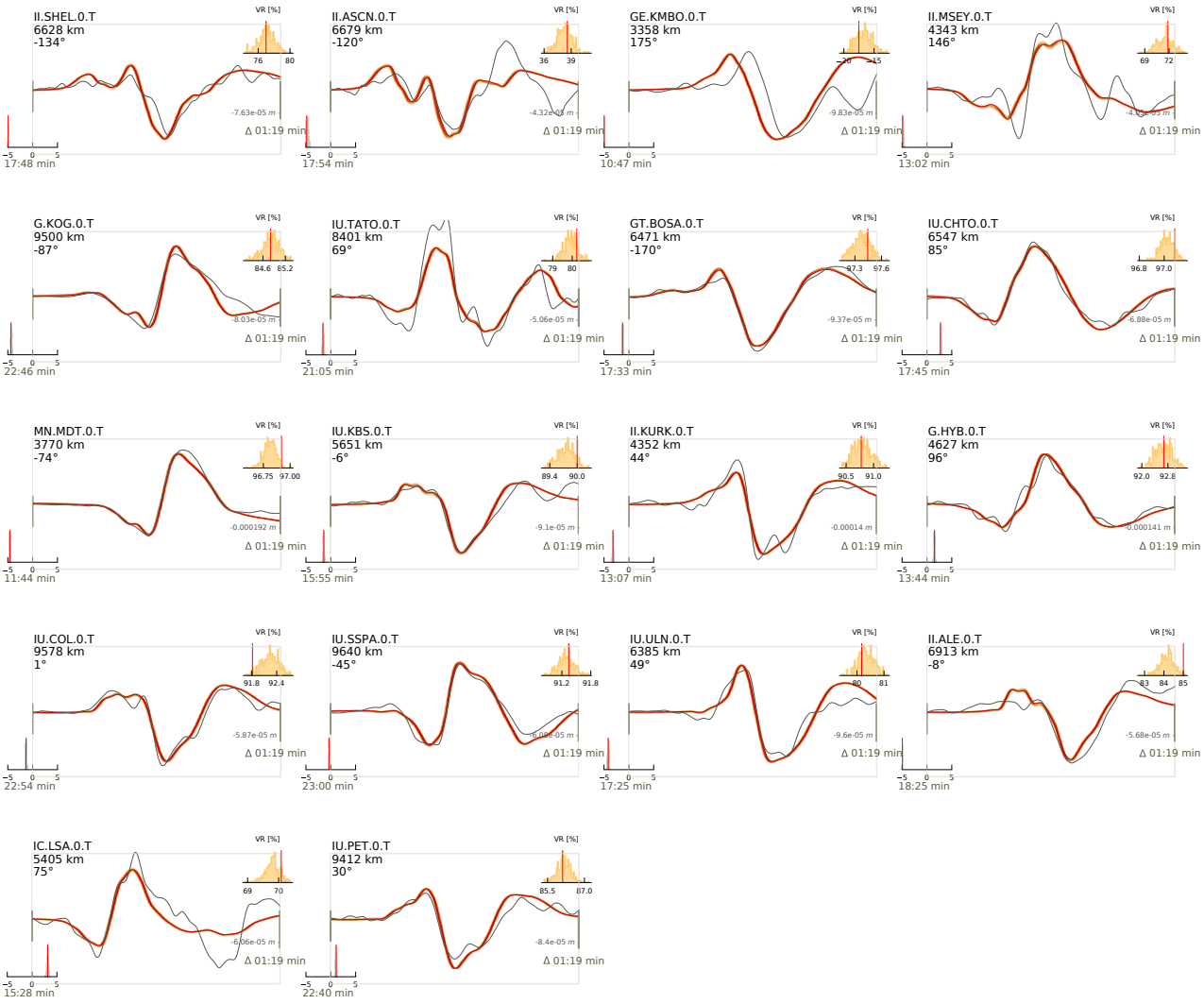

Figure S23: Three sub-faults: Waveform fits for the finite-fault inference of the 1995 Gulf of Aqaba earthquake. Solid gray lines show the filtered (0.01-0.5 Hz) data of the transverse component tapered around the S-wave arrival. Further details are given in the caption of Fig. S13.

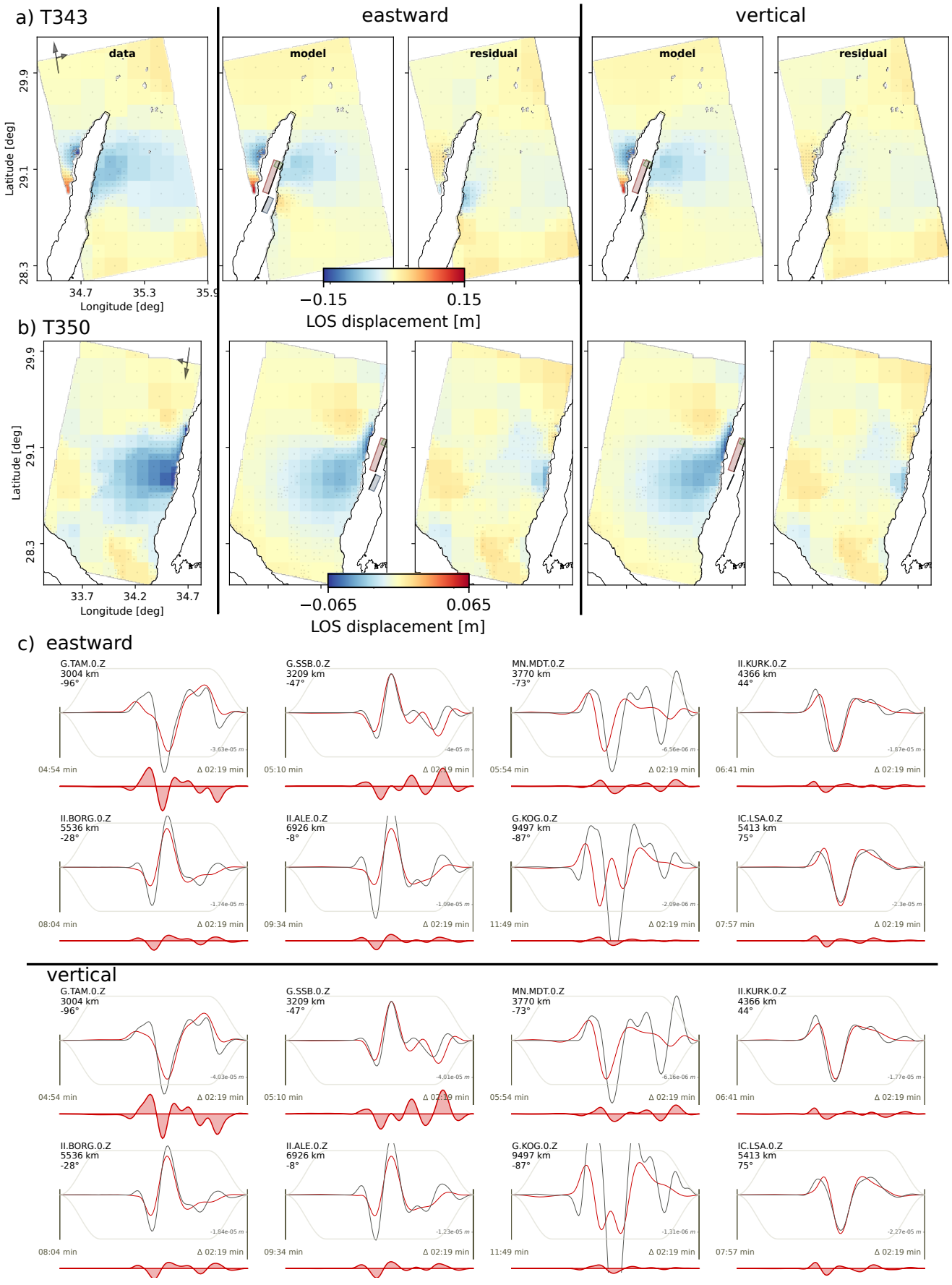

Figure S24: InSAR data fits for the track T343 a) and T350 b) for an eastward-dipping (left) and vertical (right) southern segment. Further details are given in the caption of Fig. S11.

c) Waveform fits for the finite-fault inference of the 1995 Gulf of Aqaba earthquake. Solid gray lines show the filtered (0.01-0.1 Hz) data of the vertical component tapered around the P-wave arrival for an eastward-dipping (top) and vertical (bottom) southern segment. Further details are given in the caption of Fig. S13.

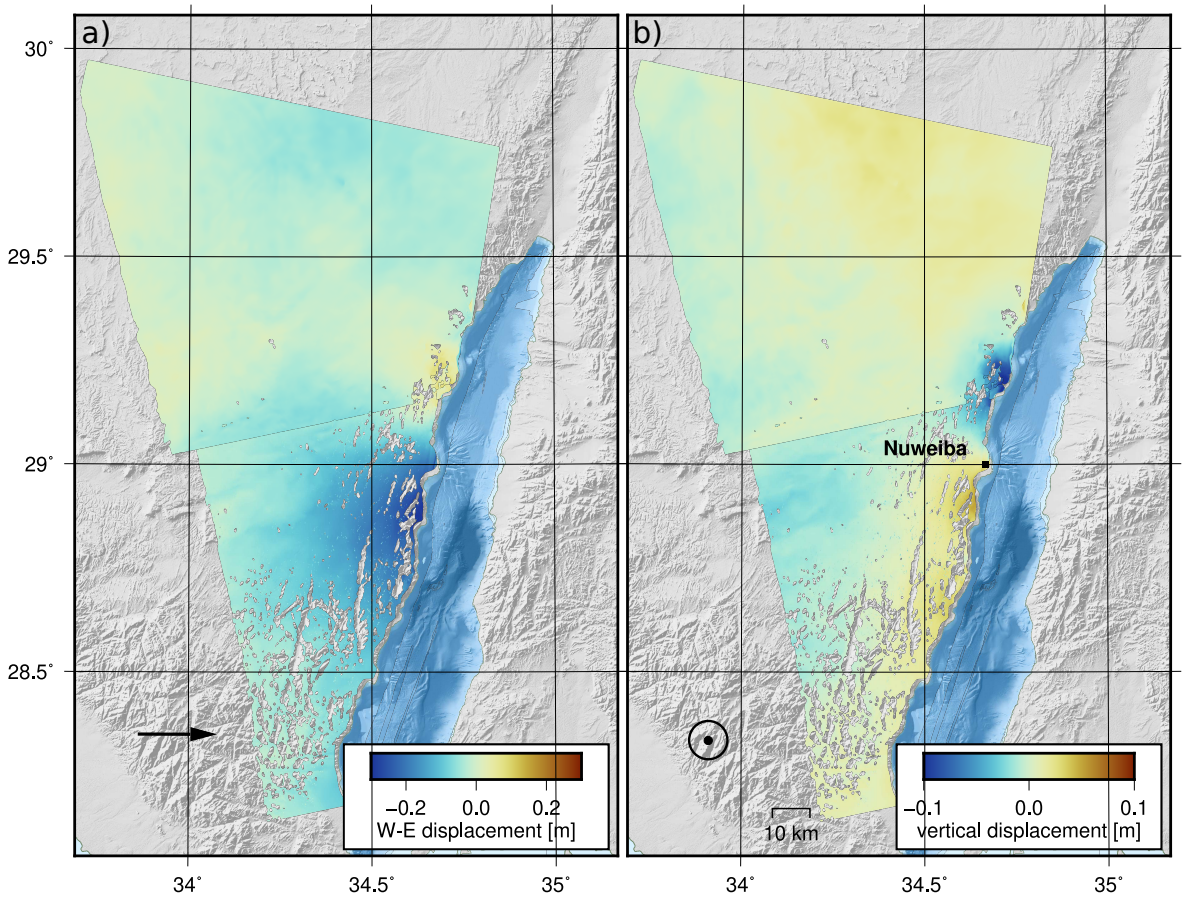

Figure S25: Decomposition of the LOS displacements from tracks 343 and 114 (Fig. 2) into a) West-East horizontal (East-ward positive) and b) near-vertical displacement (upward positive) components.

References

Baer, G., Funning, G. J., Shamir, G., and Wright, T. J. (2008). The 1995 November 22, M w 7.2 Gulf of Elat earthquake cycle revisited. *Geophys, J. Int.*, 175(3):1040–1054.

Baer, G., Shamir, G., Sandwell, D., and Bock, Y. (2001). Crustal deformation during 6 years spanning the M w = 7.2 1995 Nuweiba earthquake, analyzed by Interferometric Synthetic Aperture Radar. *Israel Journal of Earth Sciences*, 50(1):9–22.

Hofstetter, A., Thio, H. K., and Shamir, G. (2003). Source mechanism of the 22 / 11 / 1995 Gulf of Aqaba earthquake and its aftershock sequence. *J. Seismolog.*, 7:99–114.

Klinger, Y., Michel, R., and Avouac, J.-P. (2000). Co-seismic deformation during the Mw 7.3 Aqaba earthquake (1995) from ERS-SAR interferometry. *Geophys. Res. Lett.*, 27(22):3651–3654.

Klinger, Y., Rivera, L., Haessler, H., and Maurin, J.-c. (1999). Active Faulting in the Gulf of Aqaba : New Knowledge from the Mw 7 . 3 Earthquake of 22 November 1995. *Bull. Seismol. Soc. Am.*, 89(August):1025–1036.

Pinar, A. and Türkelli, N. (1997). Source inversion of the 1993 and 1995 Gulf of Aqaba earthquakes. *Tectonophysics*, 283(1-4):279–288.

Shamir, G., Baer, G., and Hofstetter, A. (2003). Three-dimensional elastic earthquake modelling based on integrated seismological and InSAR data: the M w = 7.2 Nuweiba earthquake, gulf of Elat/Aqaba 1995 November. *Geophys, J. Int.*, 154(3):731–744.